



HAL
open science

Non-destructive inspection of initial defects of PA6.6-GF50/aluminum self-piercing riveted joints and damage monitoring under mechanical static loading

Amandine Gay, Jean-Michel Roche, Patrick Lapeyronnie, Frederic Valiorgue,
Philippe Bertrand

► To cite this version:

Amandine Gay, Jean-Michel Roche, Patrick Lapeyronnie, Frederic Valiorgue, Philippe Bertrand. Non-destructive inspection of initial defects of PA6.6-GF50/aluminum self-piercing riveted joints and damage monitoring under mechanical static loading. *International Journal of Damage Mechanics*, 2016, 10.1177/1056789516648370 . hal-01461497

HAL Id: hal-01461497

<https://hal.science/hal-01461497>

Submitted on 4 Oct 2021

HAL is a multi-disciplinary open access archive for the deposit and dissemination of scientific research documents, whether they are published or not. The documents may come from teaching and research institutions in France or abroad, or from public or private research centers.

L'archive ouverte pluridisciplinaire **HAL**, est destinée au dépôt et à la diffusion de documents scientifiques de niveau recherche, publiés ou non, émanant des établissements d'enseignement et de recherche français ou étrangers, des laboratoires publics ou privés.



Distributed under a Creative Commons Attribution 4.0 International License

Non-destructive inspection of initial defects of PA6.6-GF50/aluminum self-piercing riveted joints and damage monitoring under mechanical static loading

Amandine Gay^{1,2}, Jean-Michel Roche³,
Patrick Lapeyronnie³, Frédéric Valiorgue² and
Philippe Bertrand²

Abstract

A self-piercing riveting process is used to join a thermoplastic composite sheet of PA6.6-GF50 with an aluminum alloy sheet 5182 O. Two shapes of self-piercing rivet are tested: the countersunk rivet and the button head rivet. Non-destructive inspections by pulse thermography and post-mortem cross-section observations are made to assess the damage that might have occurred during the rivet piercing process. The manufacturing defects are characterized and the possible causes for their emergence are explained. Then, single-lap joint tests were carried out to determine the best joint in terms of its mechanical strength. These tests were also instrumented by various monitoring techniques such as passive thermography, digital image correlation, and acoustic emission to clarify the joint damaging behavior. Non-destructive inspections by pulse thermography are finally correlated with the thermal fields acquired by passive thermography during the mechanical test to improve the understanding of the damage mechanisms and their criticality.

Keywords

Non-destructive testing, polymer-matrix composites (PMCs), joining, self-piercing riveting, damage detection

¹Renault, Guyancourt, France

²Laboratoire de Tribologie et Dynamique des Systèmes, Université de Lyon, Saint-Etienne, France

³Composite Materials and Structures Department, ONERA, Châtillon, France

Corresponding author:

Amandine Gay, Laboratoire de Tribologie et Dynamique des Systèmes, Université de Lyon, CNRS UMR5513 ECL/ENISE, 58 rue Jean Parot, 42023 Saint-Etienne, Cedex 2, France.

Email: gay.amandine@gmail.com

Introduction

Environment regulations related to CO₂ emissions involve the development of lightweight structures in the automotive industry. Thanks to their good stiffness to weight ratio, composites can be used to replace some metal components for weight reduction purposes. This raises the question of how to join the new composite parts with metal parts.

Adhesive bonding may be a good option for multi-materials joining. For instance, Arenas et al. (2013) and Seong et al. (2008) join aluminum alloy with CFRP by adhesive bonding. However, this technique requires surface preparation and curing cycles implying a long processing time. Other industrial problems are the structure retaining position during the curing cycles and the difficulty in the process control. So far, no non-destructive technique has been proposed to properly certify an adhesive bonding structure.

Another solution is to use mechanical fasteners. But this option still has a number of disadvantages for automotive industry as summarized by Ageorges et al. (2001): drilling holes involves no sealing, production cycle time increase, geometry issue, etc. The solution proposed in this study is to use a self-piercing rivet as a mechanical fastener (Figure 1). The main advantage is that it does not require a pre-drilled hole which enables to have short production times, cost savings and to avoid geometry issues. Other advantages can be noted: good joint shear strength, high joint fatigue performance, no surface pre-treatment, no fume emission, low noise, etc. Several works demonstrated that fiber reinforced thermoset composite/metal joining by self-piercing riveting (SPR) is possible: Fratini and Ruisi (2009) tested fiber glass reinforcement composite whereas Di Franco et al. (2010, 2013) tested carbon fiber reinforced composite. Some authors studied several key parameters of the SPR process and their influence on the joint geometry and mechanical strength: the die profile (Pickin et al., 2007), the riveting force, the geometrical properties of the rivet (Settineri et al., 2010), the distance between two rivets (Di Franco et al., 2012).

However, no matter how optimized it is, the SPR process still involves fiber cutting, delamination or diffuse damage in the composite plate. Even though the need for non-destructive data has been stated for a while (He et al., 2008), in order to prevent dramatic premature failures, little information is available in the literature on this topic. Quite recently though, some attempts were made to inspect composite self-piercing rivet structures by classic ultrasonic scans by Ueda et al. (2012): delamination was detected around the rivet, right after the piercing process, and after fatigue tests. The geometrical extent of such delamination was around a few millimeters. Meschut et al. (2014) used volumetric computed tomography scan to detect delamination around a punched hole in carbon fiber reinforced plastic. The limitation is that all metal parts must be avoided in the scan.

In the present study, non-destructive testing (NDT) is performed on PA6.6-GF50/5182 aluminum joints, fastened by SPR, right after the manufacturing process. Their damaging behavior is then monitored under static loading during single-lap joint (SLJ) tests. This test is widely used to evaluate

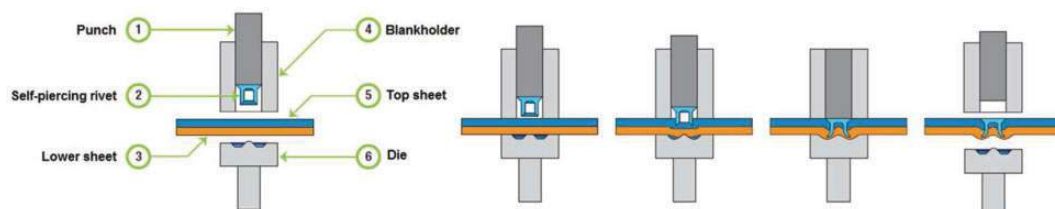


Figure 1. Self-piercing riveting process.

the mechanical strength of the joint in bonded assemblies (Comer et al., 2013) and is thus chosen here, since the configurations are quite similar to each other. Additional inspection is also made after the mechanical test.

The ultrasonic technique by immersion can be commonly used for damage detection in polymer composites (Garnier et al., 2011; Kuhn et al., 2012; Marguerès et al., 2000; Marguères and Meraghni, 2013). To avoid any wet aging that might affect the resin over the lifetime of the riveted assemblies, ultrasonics measurements by immersion were not considered in favor of active infrared thermography (a standard flash excitation system is used). Thermal active inspections aim at detecting the damage created inside the composite sheet by the rivet piercing and/or by the mechanical loading; comparisons with cross-section observations are made. Thermography is also used in its passive mode, as an in situ monitoring technique, in order to locate intern heat sources appearing at various load levels during the SLJ test and then to assess the damage scenario of the structure. Other monitoring techniques are used, such as digital image correlation (DIC) which provides strain fields and acoustic emission (AE). The cross-correlation of experimental data obtained from these independent techniques enables to provide quantitative, consistent information about the damage threshold of the structure and its successive behavior regimes (elastic, damaging), which is essential for dimensioning purposes and validation of the required mechanical properties.

Materials and methods

Materials

The SLJ configuration is chosen as it is one of the simplest tests, representative of the real loadings applied to this assembly. The overlap length is 38 mm and the self-piercing rivet is located in the center of the overlap. Sheets of 125 × 38 mm are prepared, with a thickness of 2 mm for both composite and aluminum parts. The upper sheet is a polyamide 6.6 resin reinforced with 50% glass fibers (balanced 8H satin weave) called PA6.6-GF50; the bottom sheet is an aluminum alloy AA5182-O. The mechanical properties of the materials are presented in.

Experimental SPR process

The connection with self-piercing rivets is performed by an electric machine (Emhart-Tucker), the characteristics of which are a maximum load of 80 kN and a riveting time equal to 2 s.

The self-piercing process is shown in Figure 1. For the first step, the top sheet (composite) and the lower sheet (aluminum) are clamped together between the die and the blank holder. This configuration is chosen because the aluminum deformation capacity is higher than the one of the composite. Then, the semi-tubular rivet is pushed by the punch and it pierces the top sheet. The lower sheet begins to be deformed over the die. The self-piercing rivet flares into the lower sheet due to the die shape to form a mechanical interlock. The lower sheet forms a button on the underside. Finally, the punch and the blank holder rise. The joint is then removed.

The mechanical connections are made by 5 mm diameter self-piercing rivets (Böllhoff Company). Two rivet shapes are tested: the first one has a button head whereas the second has a countersunk head, as shown in Figure 2.

The countersunk self-piercing rivet is traditionally used in the automotive industry for metallic joints. However, the higher joint strength is expected for the button head rivet because this shape is recommended for thermoplastic materials.

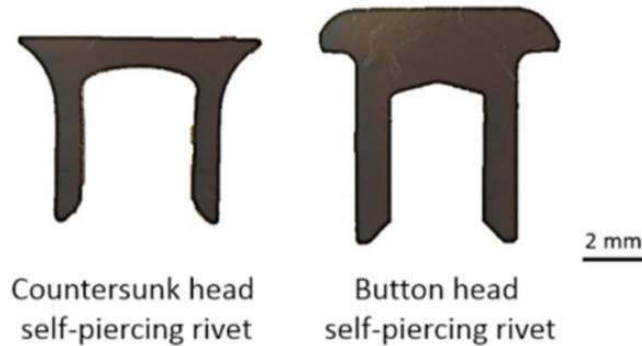


Figure 2. Cross-section of self-piercing rivet shapes.

Non-destructive techniques for damage inspection and monitoring

Non-destructive inspection techniques and processing methods. Pulse thermography experiments are carried out to inspect the joint right after the riveting process and after the SLJ mechanical tests. This choice is justified by the fact that it is a non-contact and non-invasive technique. A 6 kJ thermal impulsion is generated during 4 ms, by a system of two Elinchrom flash lamps. A FLIR X6540sc infrared camera is used for the acquisition of the surface temperature. The camera runs in the mid-wavelength infrared range (between 1.5 and 5 μm), with a space resolution of 640×512 pixels and a thermal sensitivity of 20 mK. An 18 mm extension ring is screwed on a 50 mm optical lens to focus the observation around the rivet. Images are acquired at a rate of 50 frames per second, over 30 s, duration which seems appropriate for the studied structures, given their thicknesses and their postulated thermal properties.

The post-processing of the thermal images is based on the thermographic signal reconstruction (TSR) method, initially proposed by Shepard, and extended by ONERA for automated and fast inspections (Roche et al., 2014; Shepard, 2001). Each pixel of the acquired images is processed following four steps:

- subtraction of the time-average images before the thermal pulse, in order to deal with relative temperature variations ΔT ;
- normalization by the first post-flash image, in order to limit the effects of surface inhomogeneities due to non-perfect flash illumination;
- fitting of the time-evolution of the temperature variations by logarithmic polynomials of degree 7, which can be justified by the fact that the expected behavior of ΔT is linear in a log/log scale;
- observation of the coefficient images and of the logarithmic derivatives images, that provide optimized contrasts between defects and the zone sound.

For one given sample, final thermal damage maps can be compared to the initial ones and to passive thermography images acquired during the SLJ tests (see “Non-destructive monitoring techniques during mechanical testing” section).

In addition to the initial pulse thermography inspections, Tescan scanning electron microscopy is used to observe the composite cross-section and validate the damaged areas detected in the thermal results. The magnification of the microscopy can be ranged from 50 to 5000.

Non-destructive monitoring techniques during mechanical testing. The SLJ tests are performed on a 150 kN electromechanical Zwick machine. The loading is applied to the structure with a displacement speed of 0.5 mm/min up to failure. As a reminder, the coupon is composed of two sheets (125 x 38 mm²), which are assembled at their ends by a single rivet, leading to an overlap length of 38 mm. The ratios are then set to $W/D=7.6$ and $e/D=3.8$, where W is the coupon width, D the rivet diameter, and e the distance from the rivet center to the coupon end. The vertical loading axis is aligned with the composite/aluminum interface plane thanks to the use of fitted wedges in the mechanical jaws. The composite plates are systematically positioned in the warp direction. No end tab is bonded on the specimens. No anti-bending device is used in order to be closer to real loadings in riveted structures. Two series of three tests are performed and each series is for both type of rivet (countersunk head and button head). The test is multi-instrumented by the infrared camera and two optical 4Mpx cameras used for stereo-DIC, all of them pointing at the composite side of the structure. A piezoelectric sensor is placed in contact with the composite, at its bottom, for AE monitoring.

The acquisition parameters are chosen as follows:

- passive thermography: continuous acquisition all along the SLJ test, with a frequency of 10 frames per second;
- stereo-DIC: continuous acquisition all along the SLJ test, with a frequency of one image every second;
- AE: acquisition of acoustic events occurring during the SLJ test, with a 40 dB threshold.

The passive thermal monitoring is used to identify any change of thermal behavior that might be associated with the appearance of damage, even diffuse one, like at the beginning of the test for damage threshold estimation. It also enables the detection of local heat sources that may be the signatures of major damage events (Balageas et al., 2008).

The correlation system is composed of two cameras, a LED light and a commercial calculation tool with correlation algorithms (Vic-3D from Correlated Solutions). The cameras are monochromatic AVT Pike F421-B ones with a 2048 × 2048 px definition and a resolution of 50 μm/px.

The AE system is composed of a sensor set on the composite with a silicone bond on the opposite face of the speckle pattern for the DIC, a preamplifier with a 40 dB threshold and an acquisition tool (AEWin from Mistras Group). Data acquired by the acoustic sensor can be treated as instantaneous amplitude peaks, signatures of individual damaging events, or as cumulative energy, preferentially used to determine a damage threshold.

The cross-correlation between those three experimental acquisition systems enables to improve the knowledge and understanding of the mechanical damage behavior of the studied structures, in order to validate the rivet piercing manufacturing process.

Experimental results

This section is dedicated to the experimental results acquired during the three following steps: initial micrographic cross-section observations and pulse thermography tests to detect possible manufacturing defects; SLJ tests, monitored by the previously introduced techniques (passive thermography, DIC and AE); final pulse thermography tests to locate the most critical post mechanical loading damage. All experiments are carried out for three samples by rivet configuration (button head and countersunk head), in order to ensure the repeatability of the tests and of the obtained results.

Initial inspection and analysis of the manufacturing defects

Post-mortem micrographic cross-section observations. In addition to the pulse thermography tests, it was possible to analyze some post-mortem micrographic observations (Figure 3). The composite damage located at the outside rivet interface may have an influence on the joint behavior because the joint failure may occur at this location. Figure 3(a) is a magnification of the composite section at the left side of the self-piercing rivet. Small defects are visible, which should not be detected by non-destructive inspections given their geometric extensions lower than 1 mm. This point will be checked by pulse thermography tests (see “Non-destructive inspection by pulse thermography” section).

Quantitative analysis can be made based on the maximum damage length, defined as the length from the end of the rivet head to the farthest defect. A magnification is useful to identify the type of defects: there are one to three fiber breakages (Figure 3b), around four intra-laminar fiber strand delamination defects (Figure 3c), and three inter-ply delamination defects (Figure 3d) in the sample. The length of the damaged zone measured 1260 μm on average. It is first determined by the tilt of the lower sheet that causes fiber bending. This tilt is due to the lower sheet deformation over the die. The composite upper sheet is no longer supported by the aluminum lower sheet which is deformed (Figure 4a). During the self-piercing rivet flaring, the rivet head pushes the composite sheet against the lower sheet. At the end of the process, the composite sheet is deformed by bending between the rivet and the aluminum as illustrated by Figure 4(b). The damage zone is also affected to a lesser extent by the rivet shape. The damage length is 20% lower for the composite pierced by the button head rivet than for the composite pierced by the countersunk rivet due to the curvature of the rivet shape (Figure 3e).

Non-destructive inspection by pulse thermography. As illustrated in Figure 5, the homogeneity of the thermal maps, from one sample to another, tends to validate the reproducibility of the manufacturing process. No major initial defects are detected on the instantaneous temperature fields: the small-sized delaminations observed on the micrographic cross-sections are not seen, which allows the assumption that they are not critical but which plainly justifies the need for a close monitoring of the damage behavior of the samples under mechanical loading (see “Non-destructive in situ damage monitoring during mechanical testing” section). The region of interest, located around the rivet, is more closely observed with the 18 mm extension optical ring. The TSR second logarithmic derivative images, for which thermal contrasts are optimal, tend to validate the assumed homogeneity.

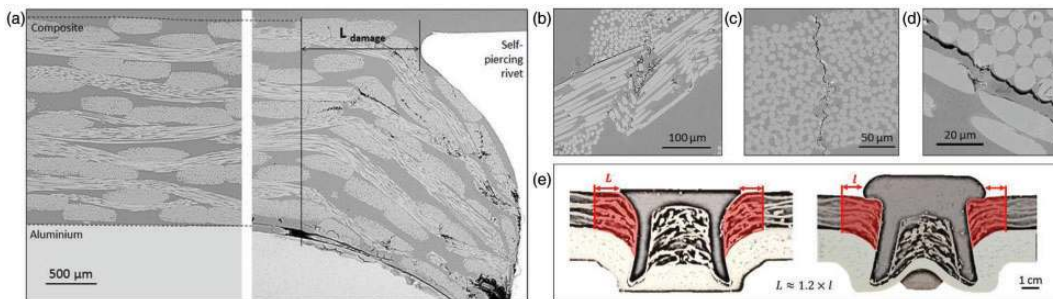


Figure 3. Composite damage caused by the rivet piercing process: (a) Cross-section of the joint, (b) focus on fiber breakage, (c) focus on intra-laminar fiber strand delamination, (d) focus inter-ply delamination, and (e) difference in terms of composite damage between the two rivet shapes.

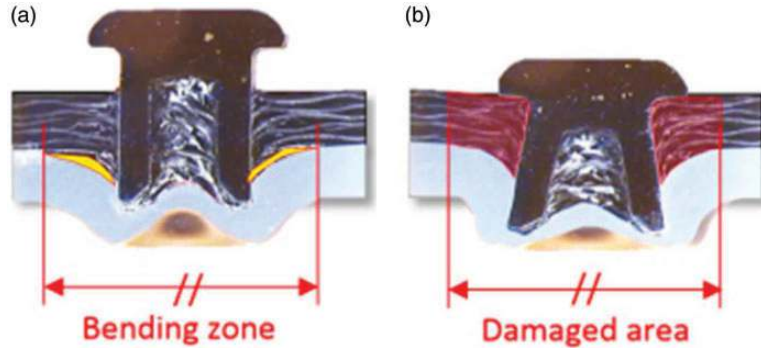


Figure 4. Cross-section of the joint (a) during the piercing and (b) at the end of the process.

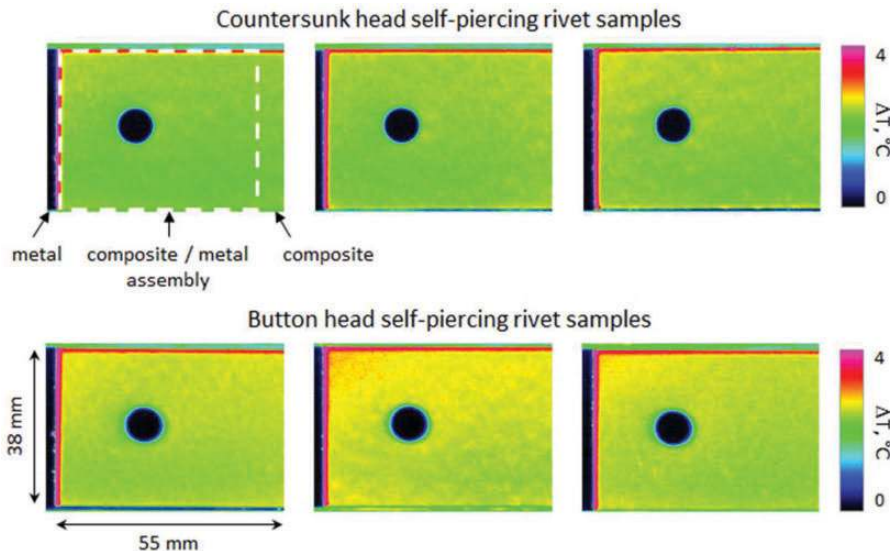


Figure 5. Instantaneous temperature fields. Time of observation: 0.5 s after the thermal flash.

However, a slight dissymmetry of the temperature variation fields between both sides of the rivet is observed (Figure 6).

A local analysis of the normalized TSR-fitted thermograms, for each side of the rivet, and of the associated first logarithmic derivatives, shows that the post-flash cooling of the structure is slower on the left of the rivet, that is to say close to the composite edge (Figure 7). The normalized thermogram obtained for the zone located on the left of the rivet, close to the composite edge, is almost similar to the theoretical one of a homogeneous material: linear decrease, with $a - \frac{1}{2}$ slope in a log/log scale, up to the rear-face. The composite / metal interface, which should be detected by a faster temperature decrease, since the thermal diffusivity of aluminum is much higher than the one of the PA6.6, is hardly seen. On the contrary, the thermograms of the region located on the right of the rivet do meet the expectations: a clear slope rupture is observed when the composite / metal interface is reached. Such variations are even more highlighted by the first logarithmic derivatives. Based on those

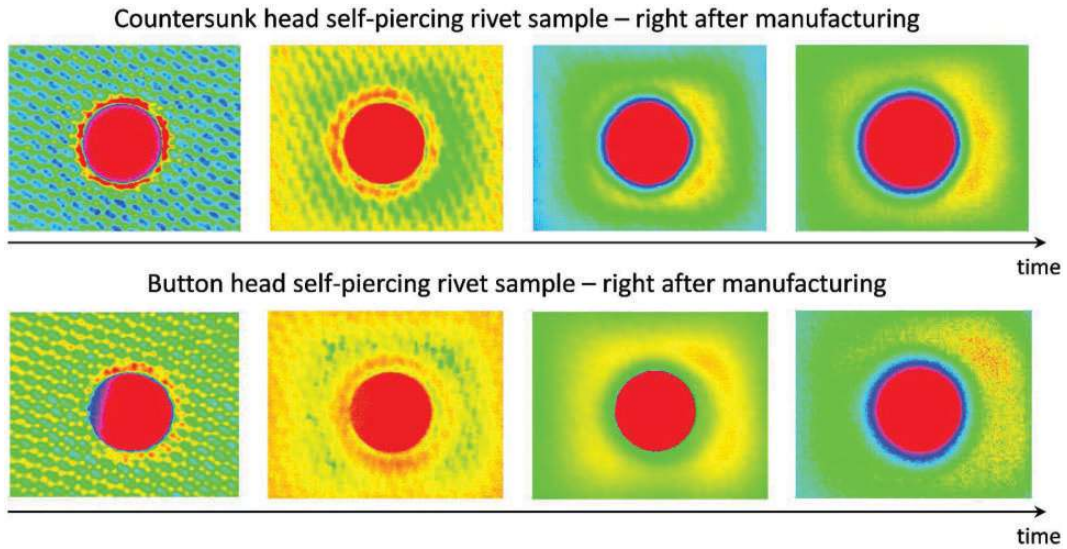


Figure 6. Second derivative-TSR maps of the rivet area close-up.

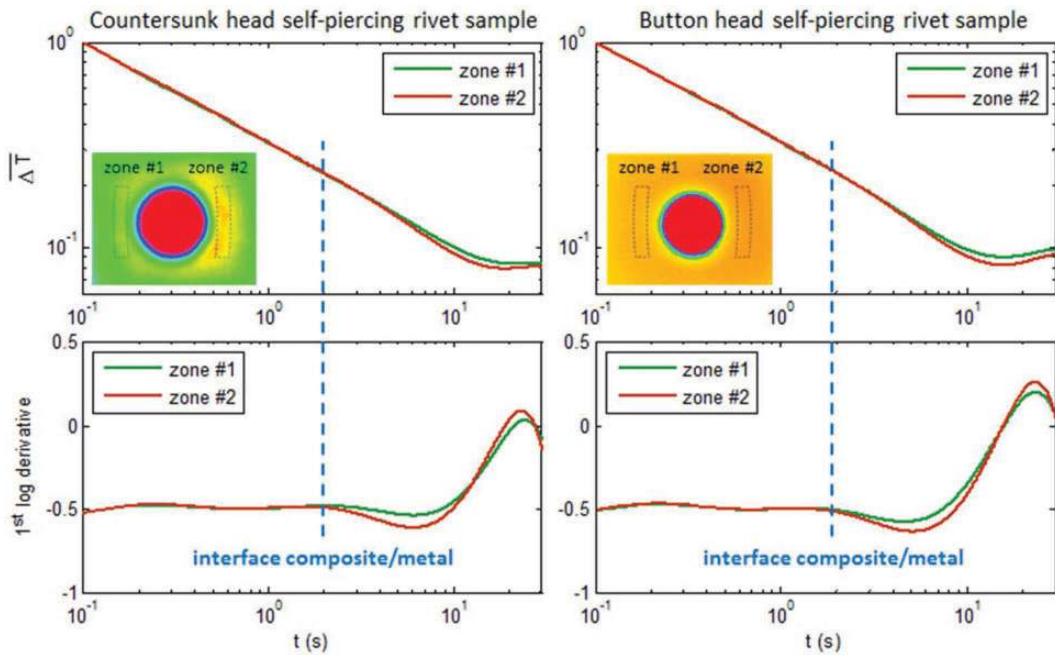


Figure 7. Time-evolutions of the TSR-fitted normalized thermograms and of the 1st logarithmic derivatives. Studied zones located on thermal 2nd logarithmic derivative images.

observations, it would appear that the composite/aluminum joint is not completely conform on the left side: the surface might be slightly curved, due to the manufacturing process and plastic strain effects. Even though this is definitely not a delamination-like defect, it still might impact the mechanical resistance of the riveted joint, by inducing a premature decohesion of the rivet.

Non-destructive in situ damage monitoring during mechanical testing

Standard mechanical monitoring. Figure 8 shows the time-evolution of the force and the failure mode of the PA6.6-GF50/aluminum self-piercing riveted joint. All force data are normalized by the maximal force value F_{MAX} reached over all mechanical tests performed on both rivet types. It clearly appears that the button head rivet joint achieves a shear strength higher by 10% than the one of the countersunk rivet joint (Figure 8a).

Once the riveted joint and jaw are set up, the load linearly increases, which is characteristic of an elastic behavior (phase #1). Afterward, the load keeps growing, non-linearly this time, up to the maximum (phase #2). Finally, the rivet is pulled out from the composite, by rotation, generating a load decrease, slow at first (phase #3), then dramatic, until the total detachment of the rivet from the aluminum sheet (phase #4). This failure mode seems to be the combination between bearing and pull-through failures, as observed for composite joints (Aktas, 2005; Kelly and Hallström, 2004; Ueda et al., 2012; US Mil-Hdbk 17 A, 1994). One part of the composite, on the upper side of the rivet (Figure 8b), is crushed (bearing) and is thus lift up, while the other part (the lower side of the rivet) follows the rivet rotation, as if the matter enters in the hole left by the rivet (pull-through). For the highest strengths, the rivet foot even begins to cut off the button on the aluminum side (Figure 8c). In the button head case, the bearing failure is even more obvious as the washer prevents the exit of the rivet.

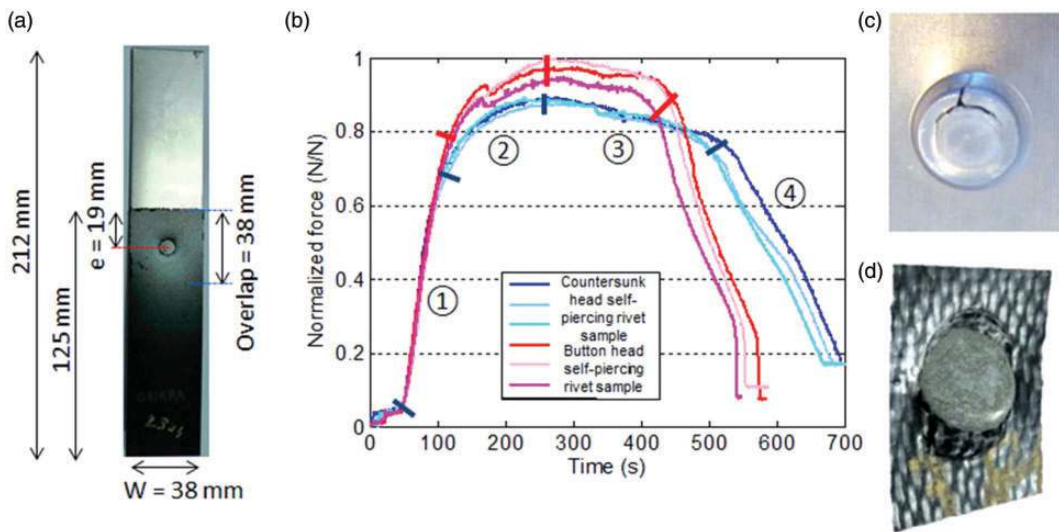


Figure 8. (a) PA6.6-GF50/aluminum joint, (b) normalized force of the PA6.6-GF50/aluminum joint, (c) failure mode on the aluminum side, and (d) failure mode on the composite side for a button head self-piercing rivet.

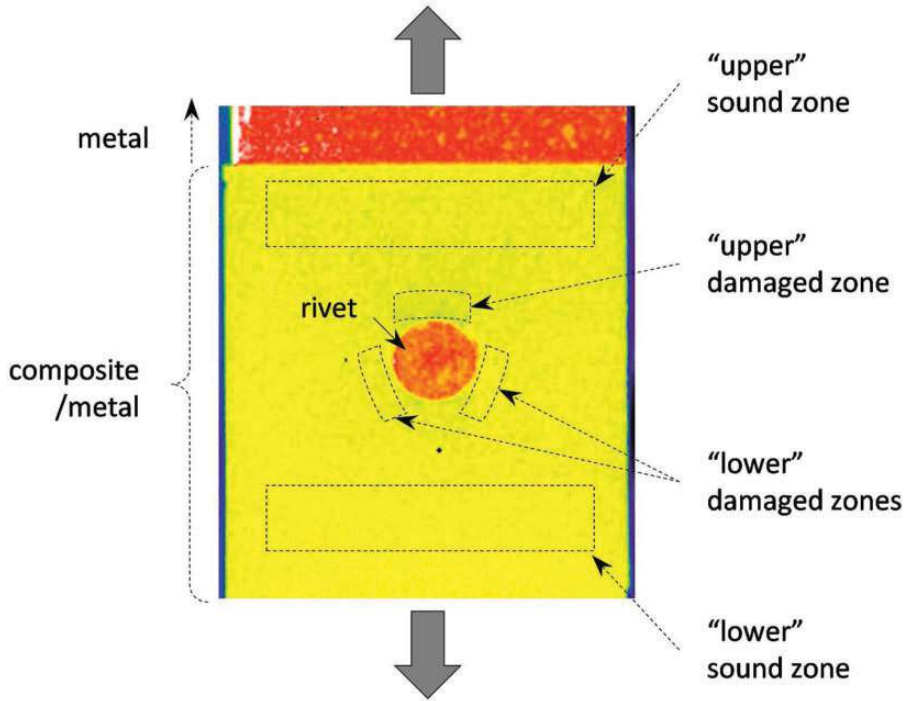


Figure 9. Location of the regions of interest thermally monitored during the SLJ test.

Passive thermal monitoring. The regions specifically observed by the infrared camera are located in Figure 9: two “sound” zones in which damage is not a priori expected; three “damaged” zones around the rivet. The time-evolutions of the temperature variations ΔT (defined as the difference between the instantaneous temperature field and the initial temperature one) are given for these zones in Figure 10.

The reproducibility of the manufacturing process is, once again, checked: for one type of rivet, the thermomechanical responses of the tested samples are quite similar to each other, particularly for the button head rivet samples. Three main thermal domains can be defined, in a general good agreement with the mechanical data: a linear decrease of ΔT , which corresponds to the mechanical phase #1; then a slow increase of ΔT , which can be associated with the beginning of the mechanical phase #2; finally, a strongly non-linear evolution of ΔT , characterized by several temperature jumps, which corresponds to the end of phase #2 and to the load decrease observed in phases #3 and #4.

The loss of linearity, both spotted on the force and temperature time-evolutions (dotted line, Figure 10), corresponds to a damage threshold, which is quite similar from one type of rivet to another, found around $0.45 \times F_{MAX}$. The first non-linearities are mainly linked to viscous effects in the composite material and to microscale, diffuse damage. Then, the local temperature rises are associated with intern heat sources that indicate the presence of severe damage, located around the rivet, as illustrated in Figure 11.

The damage scenarios that are observed for both types of riveted joints differ from each other: for the button head rivet samples, the first major damage appears quite early, characterized by a significant rise of temperature, of about half a degree, and is located right above the rivet; for the countersunk rivet samples, the thermal discontinuities are recorded close to the end of the SLJ test,

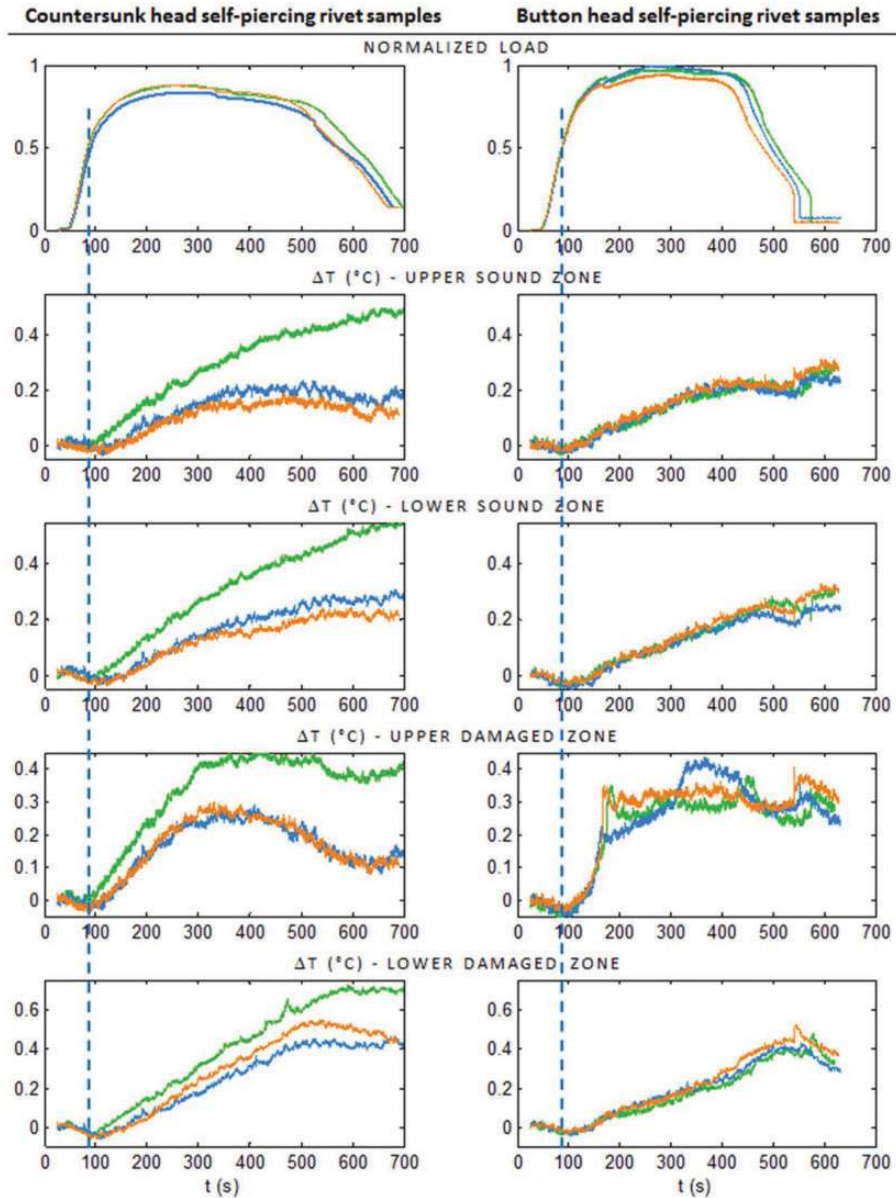


Figure 10. Time-evolutions of the temperature variations during the SLJ tests.

and the damage is located on the sides of the rivet. However, the maximum reached efforts are higher for the button head self-piercing rivet samples, which means that the major temperature jump spotted in the upper zone of the rivet does not have critical effect on the mechanical resistance. Comparisons with complementary data, from DIC and AE, are needed to analyze such phenomenon (see “Cross-correlation between experimental data” section).

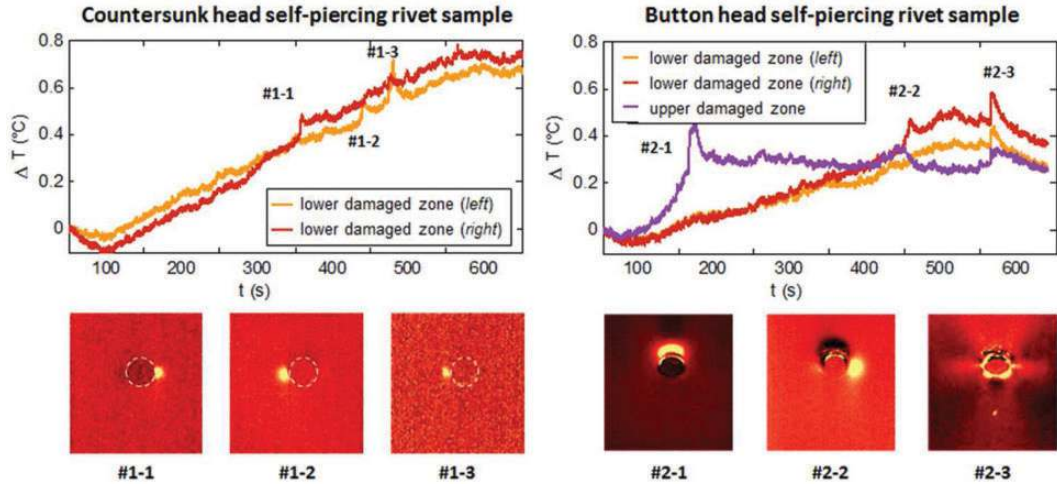


Figure 11. Heat signatures of the major damage occurring during the SLJ test.

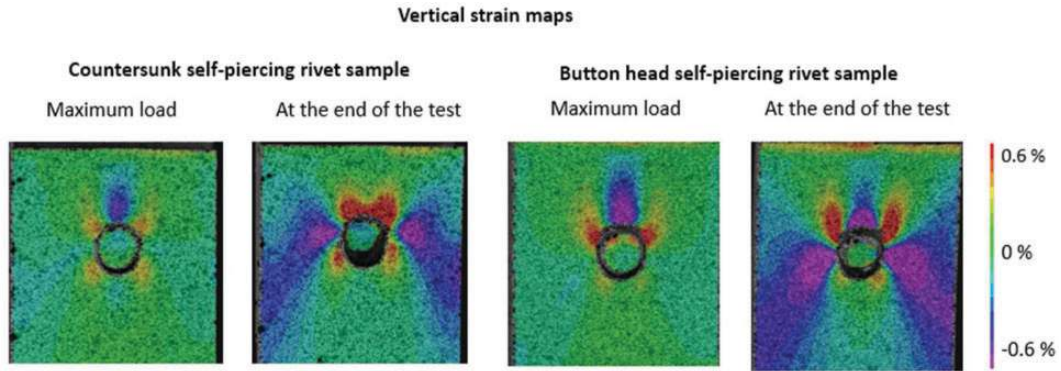


Figure 12. Vertical strain maps at the maximum load and at the end of the SLJ test.

Monitoring by stereo DIC. Data provided by DIC first show that the self-piercing rivet shape seems to affect the stress distribution around it. For button head riveted joints, the area above the rivet is permanently in vertical compression, which is due to the presence of the rivet head preventing its gradual exit from the composite, unlike what is observed for the countersunk rivet, and consequently allows a better shear strength. In the countersunk case, the progressive exit of the rivet changes the strain field with a vertical tensile area above the rivet, as the matter is free to follow the rotation.

Strain fields enable to link the previously detected local temperature rises to actual mechanical effects (Figure 12): the heat source observed right above the button head rivet (damage #2-1 in Figure 11) is due to a local compression; the other heat sources, for both rivets, are located on a horizontal crease of high deformation gradient. More thorough comparisons are made in “Cross-correlation between experimental data” section (Figures 14 and 15).

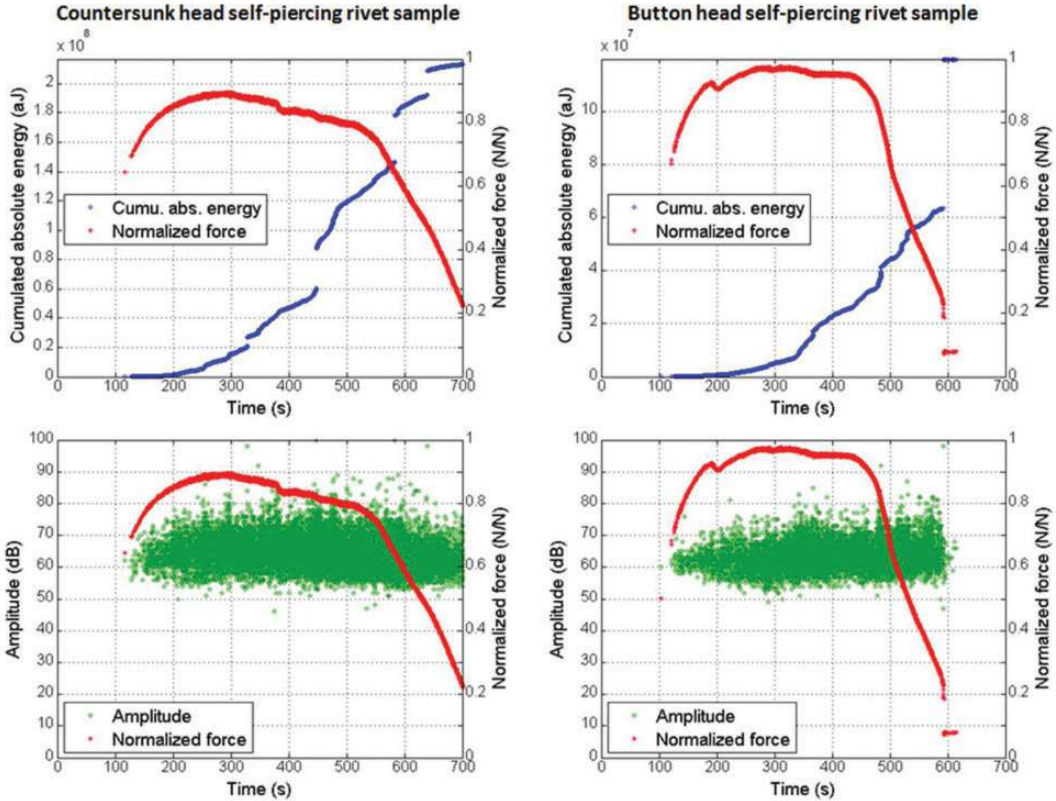


Figure 13. Acoustic measurements (amplitude peaks and cumulative energy) during the SLJ tests.

Monitoring by AE. As illustrated in Figure. 13, the acoustic activity recorded during the SLJ tests is quite similar from one type of rivet to another. The first acoustic events, mainly isolated, low-amplitude ones, appear for a high fraction of the maximum load F_{MAX} (around 0.65 for both types of riveted joints). The damage thresholds, associated with the beginning of the growth of the cumulative energy, are really too high, estimated around $0.70 \times F_{MAX}$. This value turns out to be significantly higher than what was found by passive thermography, which tends to confirm that the beginning of the heating of the composite is not associated with damage. Overall, it is also observed for both samples that most of the acoustic events are recorded after F_{MAX} that is to say during the slow decrease of the force and its final quicker drop. Moreover, the average amplitudes of the acoustic peaks are found around 60 dB, which typically corresponds to matrix cracking and delamination (Chen et al., 1992); events of higher energy (from 80 to 100 dB), which should be the signatures of fiber breaking damage, are also detected but in a much lower proportion.

The main difference between both riveted joints remains in the absolute values reached by the cumulative acoustic energy, which are about twice higher for the countersunk head rivet samples, even before F_{MAX} . This underlines the fact that the SLJ tests generate more damage in the countersunk head self-piercing rivet samples. However, the difference lies in the number of damaging events, not in their amplitude, which is quite consistent with the fact that the ratio between the respective

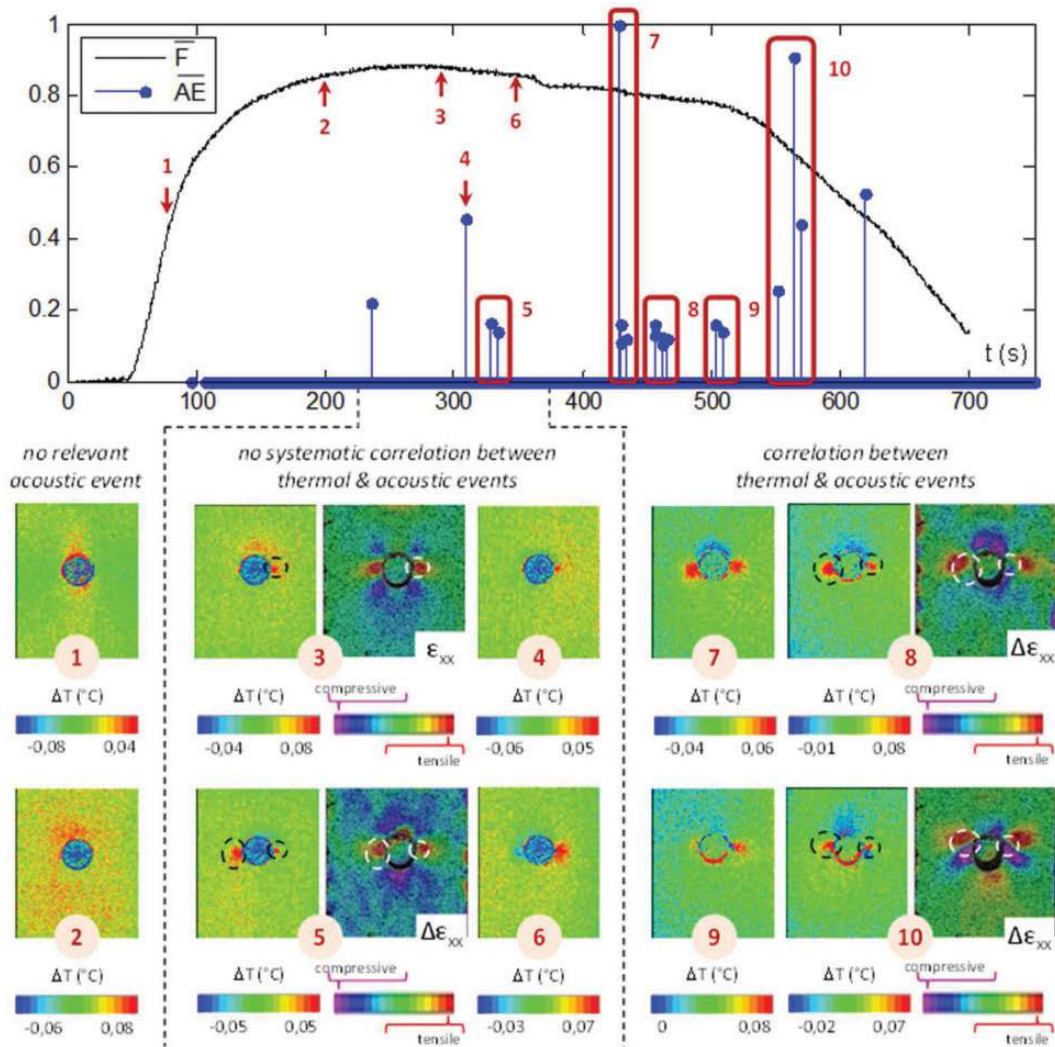


Figure 14. Countersunk head rivet in situ damage behavior under SLJ loading: cross-correlation between acoustic data, thermal and strain fields.

maximum reached loads is not that big (around 0.9, see Figure 8). This difference of events quantity is linked to the rivet head limiting its rotation and its exit, and thus the associated damaging events.

Cross-correlation between experimental data. The separate analysis of the experimental data led to the identification of several behavior domains during the SLJ tests. The standard mechanical monitoring highlighted four main phases on the time-evolution of the force: a linear increase, a non-linear one, then a slow decrease, and finally a severe drop. The thermal monitoring showed three different self-heating behaviors of the composite: a global linear cooling, followed by a slow heating, up to highly non-linear temperature variations with local peaks. Local variations of the strain fields around the rivet were spotted by DIC, especially for high values of force and during the load drop phases.

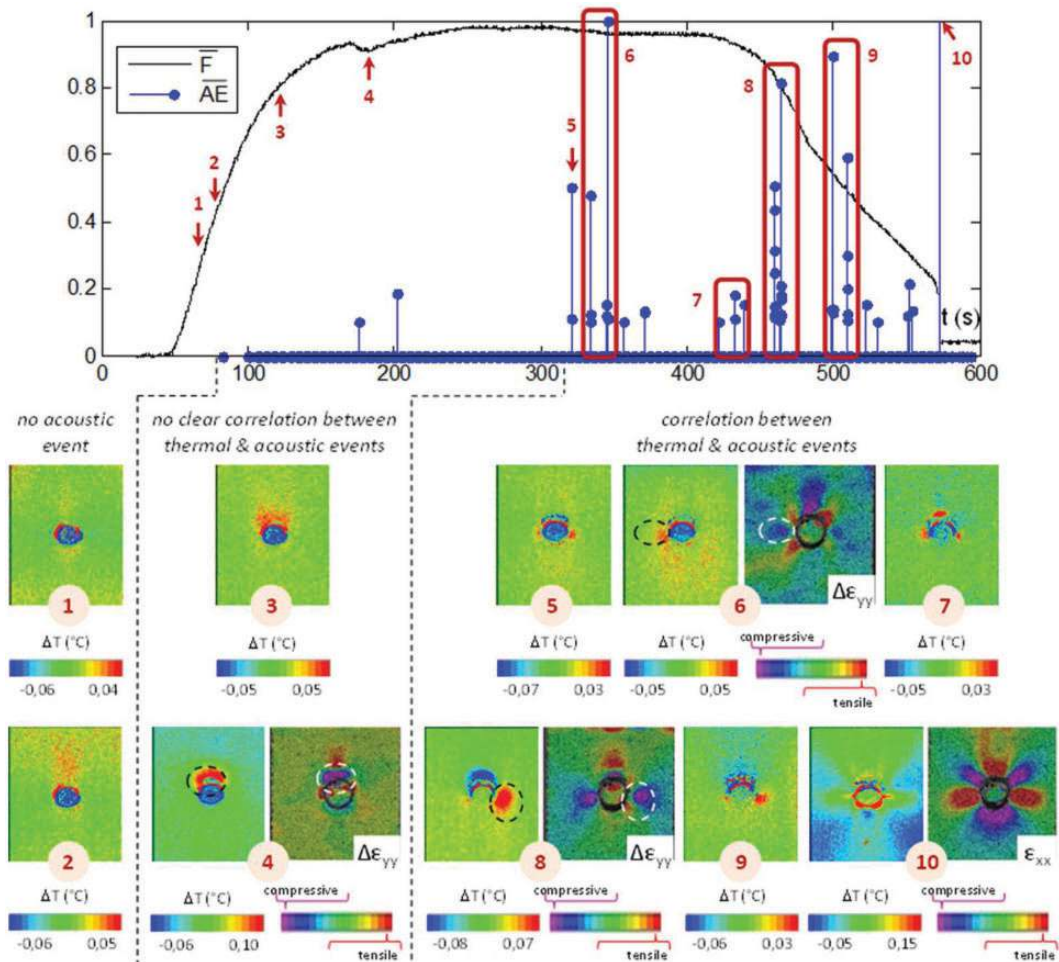


Figure 15. Button head rivet in situ damage behavior under SLJ loading: cross-correlation between acoustic data, thermal, and strain fields.

Finally, AE enabled to identify matrix cracking and delamination as the main damage mechanisms and underlined the fact that they mainly occurred after the maximum force was reached. Several damage thresholds, based on the time-evolutions of the force, of the temperature and of the acoustic activity, were determined.

The aim of this last subsection is to propose a condensed overview of the damaging behavior of both countersunk head and button head rivet samples, based on the two following representations which illustrate the cross-correlation between all these data (Figures 14 and 15).

In both figures, comparisons are made between the following data:

- the force, normalized by the maximum F_{MAX} (reached for button head rivets), as it was defined for the previous sections;
- energy of the acoustic peaks, which, for the purpose of the present analysis, was normalized by the maximum value reached for the SLJ test and then filtered so that no event of a normalized

energy lower than 0.1 would appear; for a better visual analysis, the last recorded peak, associated with the final failure of the button head rivet samples, was deliberately not taken into account for the normalization operation;

- instantaneous local temperature variation maps, obtained from the subtractions of time-sliding reference temperature fields, around the rivet;
- instantaneous absolute or relative strain fields, around the rivet.

The cross-correlation between thermal and acoustic data confirms the identification of three separate phases for the SLJ tests, identical for both types of rivet: in the first one, light heating is detected but no acoustic event is recorded, or at least no significant one; in the second one, several, clear temperature rises are locally identified while acoustic peaks are not as numerous as what might have been expected and not necessarily correlated with the heating of the composite; in the last one, the acoustic activity is fully engaged and the association of the recorded peaks and temperature jumps appears to be quite consistent.

The first phase corresponds to the linear elastic regime. A diffuse heating of the composite is observed in the upper part of the rivet, with no creation of damage, at least at a mesoscopic scale, which tends to confirm the assumption of viscous non-damaging effects. It also justifies why the threshold defined from AE data is found at a higher force than the one found with passive thermography.

The second phase is characterized by a non-linear mechanical behavior and the beginning of the rotation of the rivet which can be seen on the DIC fields: positive horizontal deformation is induced on each side of the rivet; as for the vertical deformation, it indicates that the upper zone of the rivet is in pure compression while the lower one is in tension. As a consequence, substantial temperature rises are detected around the rivet: the intern heat sources symmetrically detected on both sides of the countersunk rivet correspond to a strain gradient due to a tension/compression transition zone; the major temperature jump detected right above the button head rivet (heat source #6) is mainly due to a local compression. This latter thermal event, also spotted for the countersunk rivet but after F_{MAX} (heat source #4), is accompanied with a marked, local load drop, similar to a “bearing peak”.

The third phase, associated with the load decrease due to the progressive decohesion of the rivet from the lower sheet, is quite standard: several isolated damage events are detected by both acoustic energy peaks and local heat sources. It should be noted that depending on the nature and the depth of the damage, the thermal signature obtained on the composite surface may either be instantaneous and punctual, or progressive and diffuse because of lateral diffusion effects (Roche et al., 2015). Some heating zones are thus associated with given isolated acoustic peaks; others are associated with several acoustic peaks occurring at close time intervals. These zones can also be identified on strain fields provided by DIC: the continuing exit of the rivet by rotation keeps the composite under compression on a horizontal crease located halfway up the rivet on its sides. In the end, the damage pattern of both samples differs a bit: the lateral sides of the countersunk rivets are the most damaged; as for the button head ones, the main damage is too lateral but slightly below the rivets. Some remaining acoustic peaks do not have any signature provided by thermography or DIC, which might be due the location of the damage, outside of the observation window accessible to the cameras (in the rivet detachment from the aluminum area, for instance) or too deep inside the composite, and to its limited geometrical extents.

Non-destructive final inspection by pulse thermography

Similarly to what was initially done, the very same pulse thermography inspections are carried out on the damaged composite parts which were dissociated from the metallic parts during the SLJ test.

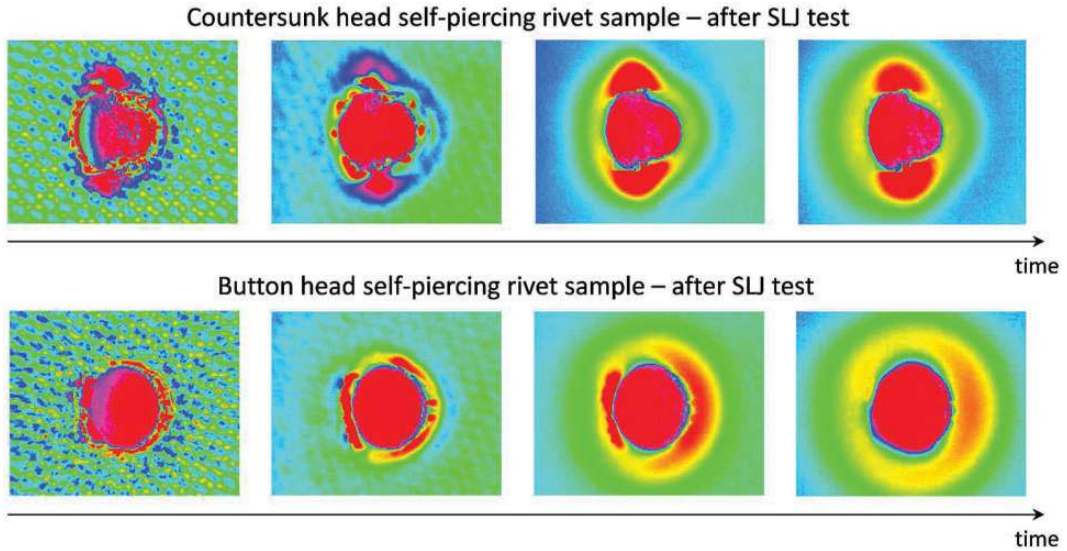


Figure 16. Second derivative-TSR maps of the samples after final mechanical failure.

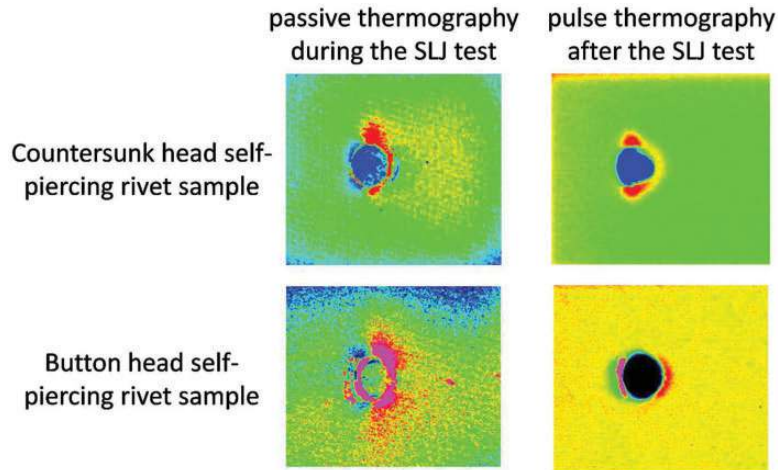


Figure 17. Comparisons between thermal maps acquired during the SLJ test by passive thermography and after the SLJ test by pulse thermography.

Severe damage is detected around the rivet, of geometrical extension similar to the rivet diameter. It is visible for early times, which indicates that it is mainly constituted of shallow defects. The countersunk head rivet samples seem to be more damaged on the sides of the rivet than the button head ones (Figure 16), which is in agreement with the previous in situ observations. More globally, the damaged zones detected by post-SLJ test pulse thermography can be linked to the ones detected during the SLJ test (Figure 17).

Table 1. Materials properties (from manufacturer datasheets).

Properties	Aluminum	PA6.6-GF50 (in warp direction)
Young modulus	71 GPa	31.2 GPa
Tensile strength	255 MPa	520 MPa
Poisson's ratio	0.33	0.17

Conclusions

In this paper, the non-destructive inspection of initial defects of PA6.6-GF50/aluminum joint by SPR was carried out, as well as the multi-instrumented monitoring of its damage behavior under static loading.

Non-destructive tests by pulse thermography and joint cross-sections have led to the validation of the SPR process because of its reproducibility and the limited introduction of defects inside the composite. The defects, such as fiber breakage and delamination, caused by the bending of the composite plate during the rivet piercing, have geometrical extents so small that none of them are detected on the thermal maps. A slight curvature of the joint is however spotted by thermography.

Comparisons between experimental data acquired during single-lap-joint tests by passive thermography, DIC and AE enabled to clarify the joint damaging behavior under shear static loading. The cross-correlation confirms for both types of rivet that the identification of three separate phases for the SLJ tests:

- The first phase corresponds to the linear elastic regime. Moreover a diffuse heating of the composite is observed in the upper part of the rivet at $0.45 \times F_{MAX}$ with no creation of damage.
- The second phase is characterized by a non-linear mechanical behavior and the beginning of the rotation of the rivet. The upper zone of the rivet is in pure compression while the lower one is in tension. The damage thresholds are estimated around $0.70 \times F_{MAX}$ by acoustic measurements. The average damage typically corresponds to matrix cracking and delamination.
- The third phase is associated with the load decrease. It is due to the progressive decohesion of the rivet from the lower sheet. Most of the damages are recorded during this phase. Several isolated damage events are detected by both acoustic energy peaks and local heat sources.

The button head rivet shape is more favorable for the joint mechanical performances than the countersunk rivet shape. Although the first damage appears quite early for the button head rivet with a significant rise of temperature, it was shown that it is not critical and the joint achieves higher strength than the one of the countersunk rivet. In addition, the SLJ test generates more damage in the composite joined by the countersunk rivet than by the button head rivet (higher cumulative absolute acoustic energy) and especially on the lateral sides of the countersunk rivet at the end of the test (passive and active thermography results). The higher joint strength of the button head rivet is explained by the stress distribution around it. The area above the button head rivet is permanently in compression (DIC results) which prevents the gradual rivet exit.

The immediate prospect of this work is to analyze the fatigue behavior of these riveted joints (Gay et al., 2015). Furthermore, a numerical study of the joint mechanical behavior seems necessary to predict the joint strength without expensive experimental tests. Another prospect for a further work deals with the damage detection in a SLJ consisting of an off-axis woven fabric PA66-GF50

composite: are the damage mechanisms, investigated in the warp direction under quasi-static tension, still the same in terms of initiation, kinetic and effects on the overall response of the SLJ?

Acknowledgments

The authors would like to thank Mr Philippe MICHEL (Renault) and Mr Pierre CHALANDON (CETIM) for their advice about guidelines. The authors also express their gratitude to Mrs Françoise PASSILLY (ONERA) for her contribution to this experimental study.

Declaration of Conflicting Interests

The author(s) declared no potential conflicts of interest with respect to the research, authorship, and/or publication of this article.

Funding

The author(s) disclosed receipt of the following financial support for the research, authorship, and/or publication of this article: Renault and CETIM.

References

- Ageorges C, Ye L and Hou M (2001) Advances in fusion bonding techniques for joining thermoplastic matrix composites: A review. *Composite Part A* 32: 839–857.
- Aktas A (2005) Bearing strength of carbon epoxy laminates under static and dynamic loading. *Composite Structures* 67: 485–489.
- Arenas JM, Alia C, Narbon JJ, et al. (2013) Considerations for the industrial application of structural adhesive joints in the aluminum-composite material bonding. *Composite Part B* 44: 417–423.
- Balageas D, Levesque P, Brunet P, et al. (2008) Thermography as a routine diagnostic for mechanical testing of composites. *Quantitative InfraRed Thermography Journal* 5(1): 45–68.
- Chen O, Karandikar P, Takeda N, et al. (1992) Acoustic emission characterization of a glass-matrix composite. *NDT & E International* 8–9(1–6): 869–878.
- Comer AJ, Katman K, Stanley WF, et al. (2013) Characterising the behaviour of composite single lap bonded joints using digital image correlation. *International Journal of Adhesion and Adhesives* 40: 215–233.
- Di Franco G, Fratini L, Pasta A, et al. (2010) On the self-piercing riveting of aluminium blanks and carbon fibre composite panels. *International Journal of Material Forming* 3: 1035–1038.
- Di Franco G, Fratini L and Pasta A (2012) Influence of the distance between rivets in self-piercing riveting bonded joints made of carbon fiber panels and AA2024 blanks. *Materials and Design* 35: 342–349.
- Di Franco G, Fratini L and Pasta A (2013) Analysis of the mechanical performance of hybrid (SPR/bonded) single-lap joints between CFRP panels and aluminum blanks. *International Journal of Adhesion and Adhesives* 41: 24–32.
- Fratini L and Ruisi F (2009) Self-piercing riveting for aluminium alloys-composites hybrid joints. *International Journal of Advanced Manufacturing Technology* 43: 61–66.
- Garnier C, Pastor M-L, Eyma F, et al. (2011) The detection of aeronautical defects in situ on composite structures using non destructive testing. *Composite Structures* 93(5): 1328–1336.
- Gay A, Lefebvre F, Bergamo S, et al. (2016) Fatigue performance of a self-piercing rivet joint between aluminium and glass fiber reinforced thermoplastic composite. *International Journal of Fatigue* 83(2): 127–134.
- He X, Pearson I and Young K (2008) Self-pierce riveting for sheet materials: State of the art. *International Journal of Materials and Product Technology* 199: 27–36.
- Kelly G and Hallström S (2004) Bearing strength of carbon fibre/epoxy laminates: effects of bolt-hole clearance. *Composites Part B* 35: 331–343.
- Kuhn E, Valot E and Herve Ph (2012) A comparison between thermosonics and thermography for delamination detection in polymer matrix laminates. *Composite Structures* 94(3): 1155–1164.

- Marguères P and Meraghni F (2013) Damage induced anisotropy and stiffness reduction evaluation in composite materials using ultrasonic wave transmission. *Composites Part A* 45: 134–144.
- Marguerès Ph, Meraghni F and Benzeggagh ML (2000) Comparison of stiffness measurements and damage investigation techniques for a fatigued and post-impact fatigued GFRP composite obtained by RTM process. *Composites Part A* 31: 151–163.
- Meschut G, Gude M, Augenthale F, et al. (2014) Evaluation of damage to carbon-fibre composites induced by self-pierce riveting. *Procedia CIRP* 18: 196–191.
- Pickin CG, Young K and Tuersley I (2007) Joining of lightweight sandwich sheets to aluminium using self-pierce riveting. *Materials and Design* 28: 2361–2365.
- Roche JM, Leroy FH and Balageas D (2014) Images of thermographic signal reconstruction coefficients: A simple way for rapid and efficient detection of discontinuities. *Material Evaluation* 72(1): 73–82.
- Roche JM, Passilly F, Leroy FH, et al. (2015) Thermal non-destructive characterization and in situ damage monitoring of a composite suspension wishbone. In: Groves R, Huntley J and Bhattacharya N (eds) *Proc. of the Photomechanics 2015 conference*. Delft: TU Delft.
- Shepard S (2001) Advances in pulsed thermography. *Thermosense XXIII Proc SPIE* 4630: 511–515.
- Seong MS, Kim TH, Nguyen KH, et al. (2008) A parametric study on the failure of bonded single lap joints of carbon composite and aluminum. *Composite Structures* 86: 135–145.
- Settinieri L, Atzeni E and Ippolito R (2010) Self-piercing riveting for metal-polymer joints. *International Journal of Material Forming* 3: 995–998.
- Ueda M, Miyake S, Hasegawa H, et al. (2012) Instantaneous mechanical fastening of quasi-isotropic CFRP laminates by a self-piercing rivet. *Composite Structures* 94: 3388–3393.
- US Mil-Hdbk 17A (1994) Chapter 7: Structural element characterization.